

12

Lumped-Element Circuits

Lumped elements have been in use in microwave circuits for more than 30 years. This chapter deals exclusively with these circuits where lumped elements, in addition to size reduction, provide distinct benefits in terms of bandwidth and electrical performance. Such circuits are classified into two categories: passive circuits and control circuits, as discussed in this chapter.

12.1 Passive Circuits

12.1.1 Filters

The basic theory of filters [1–10] is based on a combination of lumped elements such as inductors and capacitors as shown in Figure 12.1. This configuration is a lowpass filter, and we can develop a prototype design with 1- Ω input–output impedance and a 1-rad cutoff frequency. From here, it is simply a matter of scaling the g values for various elements to obtain the desired frequency response and insertion loss. In addition, other filter types such as highpass, bandpass, and band-stop merely require a transformation in addition to the scaling to obtain the desired characteristics.

At RF frequencies and the lower end of the microwave frequency band, filters have been realized using lumped elements (chip/coil inductors and parallel plate chip capacitors) and employ printed circuit techniques or PCBs to connect them. Several hybrid MIC technologies such as thin film, thick film, and cofired ceramic are being used to develop such circuits. Lumped-element filters can be implemented easily, and using currently available surface-mounted components one can meet size and cost targets in high-volume production. Due to the low

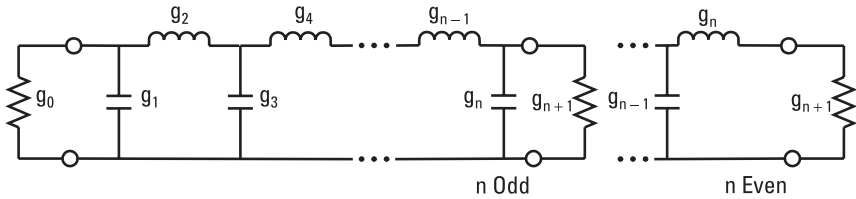


Figure 12.1 Lowpass filter prototype.

Q of inductors and capacitors, it is not possible to realize narrowband filters using MIC or MMIC technologies for some wireless applications.

The temperature sensitivity of lumped capacitors is far greater than the temperature variation in inductors. Therefore, the lumped-element filter's performance over temperature is mainly evaluated by the temperature coefficient of the capacitors [11]. The temperature sensitivity in such filters is minimized either by using only suitably designed coil inductors in which the shunt capacitance is contained in the self-resonance of the coil or thermally stable discrete capacitors.

12.1.1.1 Ceramic Lumped-Element Filters

A five-pole elliptic lowpass filter was developed [12] using thick-film printed inductors and discrete capacitors. The design goals were $f_c = 150$ MHz, passband ripple less than 1 dB, stop-band attenuation less than 40 dB at $1.5f_c$ and return loss greater than 20 dB. Figure 12.2(a) shows the design values, in which the nearest available standard values of the capacitors were used. The inductors were printed on 25-mil alumina substrate $\epsilon_r = 9.6$. Figure 12.2(b) shows the physical layout of this lowpass filter. Figure 12.3 compares the measured and simulated performance.

12.1.1.2 Superconducting Lumped-Element Filters

Conventionally, a low-loss narrowband filter having bandwidth on the order of 1% cannot be designed using a lumped-element approach due to its low Q values. However, such filters can be realized using *high-temperature superconductor* (HTS) substrates. A third-order bandpass filter with a center frequency of 1.78 GHz and 0.84% fractional bandwidth was designed and fabricated using HTS thin-film lumped elements [13]. Figure 12.4(a) shows its schematic and Figure 12.4(b) shows the layout. The filter was patterned using single-sided YBCO film on a MgO substrate. All sides, including the bottom of the substrate and the inner ends of spirals and capacitors bonding pads, were covered with silver. Components were wired together using 40- μ m-diameter gold wires and ultrasonic bonding.

Figure 12.5 shows the measured response of the filter operating at 20K. The two sets of data represent results obtained with one and two wires per

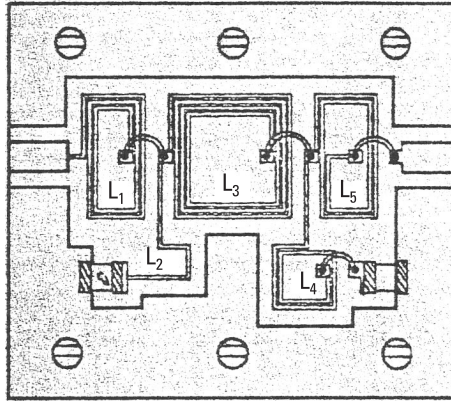
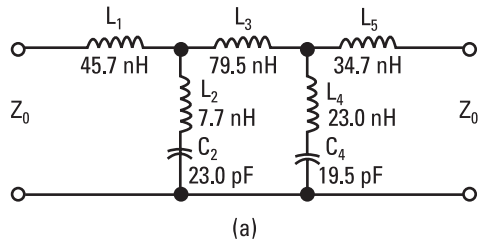


Figure 12.2 Five-pole lowpass elliptic filter: (a) schematic and (b) physical layout.

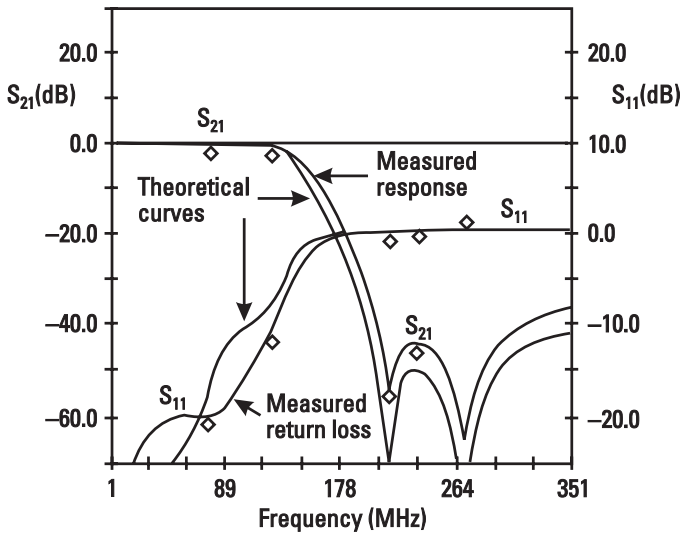


Figure 12.3 Simulated and measured performance of the lumped-element based five-pole lowpass elliptic filter.

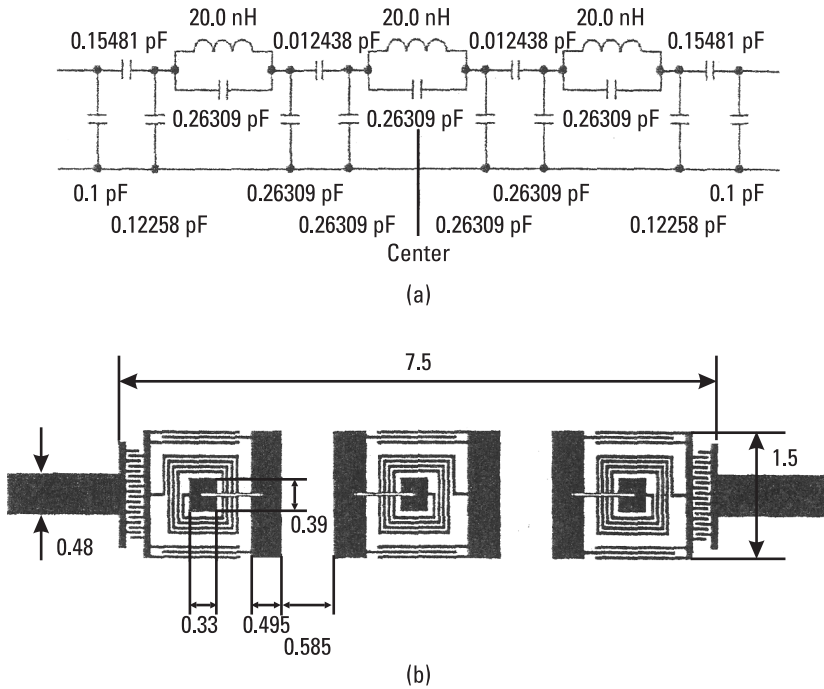


Figure 12.4 Lumped-element three-pole bandpass filter: (a) schematic and (b) physical layout. All dimensions are in millimeters. (From: [13]. © 2001 John Wiley. Reprinted with permission.)

connection. Measured insertion loss was about 1.5 dB at 1.725 GHz over 0.84% fractional bandwidth. The difference between the simulated and measured center frequency was attributed to substrate properties and etching accuracy.

Ong et al. [14] have reported a HTS bandpass filter using a dual-spiral resonator approach.

12.1.2 Hybrids and Couplers

Hybrids and couplers are indispensable components in the rapidly growing applications of microwaves in electronic warfare, radar, and communication systems. These circuits are often used in frequency discriminators, balanced amplifiers, balanced mixers, automatic level controls, and many other wireless applications. Hybrids are realized by directly connecting circuit elements, whereas couplers are realized using sections of transmission lines placed in proximity. They have four ports and have matched characteristics at all four ports; that is, over the specified frequency range the reflection coefficients are very small, usually less than 0.1, which makes them very suitable for insertion

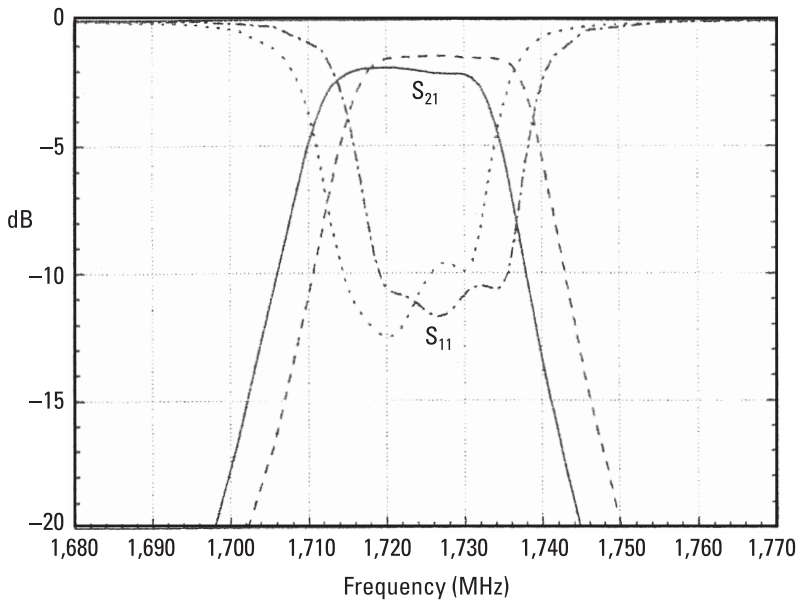


Figure 12.5 Measured performance of the three-pole bandpass filter with one wire connection (solid line: S_{21} ; dotted line: S_{11}) and two wire connection (dashed line: S_{21} ; dashed-dotted line: S_{11}). (From: [13]. © 2001 John Wiley. Reprinted with permission.)

in a circuit or subsystem. The theory of these couplers is well described in the literature [1, 4, 7, 8, 15–20]. In this section, design equations are given, and design methods for several couplers are described.

12.1.2.1 Parameter Definition

A hybrid or directional coupler can in principle be represented as a multiport network, as shown in Figure 12.6. The structure has four ports: input, direct, coupled, and isolated. If P_1 is the power fed into port 1 (which is matched to the generator impedance) and P_2 , P_3 , and P_4 are the powers available at ports 2, 3, and 4, respectively (while each of the ports is terminated by its characteristic



Figure 12.6 Four-port network.

impedance), the two most important parameters that describe the performance of this network are its coupling factor and directivity, defined as follows:

$$\text{Coupling factor (dB)} = C = 10 \log \frac{P_1}{P_3} \quad (12.1a)$$

$$\text{Directivity (dB)} = D = 10 \log \frac{P_3}{P_4} \quad (12.1b)$$

The isolation and transmitted power are given by

$$\text{Isolation (dB)} = I = 10 \log \frac{P_1}{P_4} = D + C \quad (12.2a)$$

$$\text{Transmitted power (dB)} = T = 10 \log \frac{P_2}{P_1} \quad (12.2b)$$

As a general rule, the performance of these circuits is specified in terms of coupling, directivity, and the terminating impedance at the center frequency of the operating frequency band. Usually, the isolated port is terminated in a matched load. Normally coupling, directivity, and isolation are expressed in decibels and are positive quantities. For many applications, a single-section coupler has an inadequate bandwidth. A multisection design that is a cascaded combination of more than one single-section coupler results in a larger bandwidth. The number of sections to be used depends on the tolerable insertion loss, bandwidth, and the available physical space.

12.1.2.2 90° Hybrid

The 90° hybrids use directly connected circuit elements and can be implemented either using a distributed approach or lumped elements. Because the design of the lumped-element hybrid is derived from the distributed configuration, both approaches are briefly described next.

The branch-line type of hybrid shown in Figure 12.7 is one of the simplest structures for a 90° hybrid in which the circumference is an odd multiple of λ . The geometry is readily realizable in any transmission medium. Branch-line hybrids have narrow bandwidths—on the order of 10%. As shown in Figure 12.7, the two quarter-wavelength-long sections spaced one-quarter wavelength apart divide the input signal from port 1 so that no signal appears at port 4. The signals appearing at ports 2 and 3 are equal in magnitude, but out of phase by 90°. The coupling factor is determined by the ratio of the impedance of the shunt (Z_p) and series (Z_r) arms and is optimized to maintain proper match

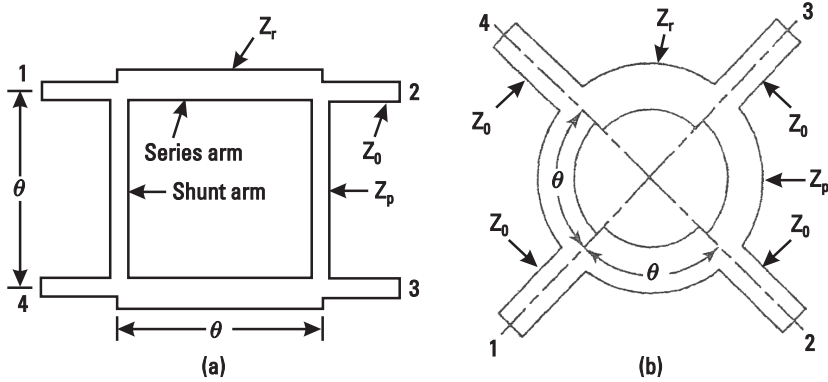


Figure 12.7 (a, b) A 90° hybrid configuration.

over the required bandwidth. In terms of Z_r and Z_p , the scattering parameters of a branch-line coupler are given by

$$S_{21} = -j \frac{Z_r}{Z_0}, \quad S_{31} = -\frac{Z_r}{Z_p}, \quad S_{41} = 0 \quad (12.3a)$$

For a 90° lossless matched hybrid, the following conditions hold:

$$|S_{21}|^2 + |S_{31}|^2 = 1$$

or

$$\left| \frac{Z_r}{Z_0} \right|^2 + \left| \frac{Z_r}{Z_p} \right|^2 = 1 \quad (12.3b)$$

For 3-dB coupling, the characteristic impedances of the shunt and series arms are Z_0 and $Z_0/\sqrt{2}$, respectively, for optimum performance of the coupler, with Z_0 being the characteristic impedance of the input and output ports. For most applications $Z_0 = 50\Omega$, thus shunt and series arms lines have characteristic impedances of 50Ω and 35.36Ω , respectively.

In MMICs, lumped capacitors can be easily realized and have become attractive in reducing the size of passive components. Reduced-size branch-line hybrids that use only lumped capacitors and small sections of transmission lines (smaller than $\lambda_g/4$) have also been reported [21]. The size of these hybrids is about 80% smaller than those for conventional hybrids and is therefore quite suitable for MMICs.

The lumped element 90° hybrid can be realized in either a *pi* or *tee* equivalent network. In MMICs, a *pi* network is preferred to a *tee* network because it uses fewer inductor elements with lower Q and occupies more space. The bandwidth of these couplers can be increased by using more sections of *pi* or *tee* equivalent networks, that is, two sections of 45° or three sections of 30° , to realize 90° sections or by properly selecting highpass and lowpass networks [22, 23]. Generally two to three sections are sufficient to realize a broadband 90° hybrid.

In the lumped-element implementation, each transmission line shown in Figure 12.7 is replaced by an equivalent *pi* lumped-element network as shown in Figure 12.8. The values of lumped elements are obtained by equating $ABCD$ -matrix parameters for both these structures. The $ABCD$ -matrix of a lossless transmission line section of characteristic impedance Z_r and electrical length θ is given by

$$\begin{pmatrix} A & B \\ C & D \end{pmatrix} = \begin{bmatrix} \cos \theta & jZ_r \sin \theta \\ j \frac{1}{Z_r} \sin \theta & \cos \theta \end{bmatrix} \tag{12.4}$$

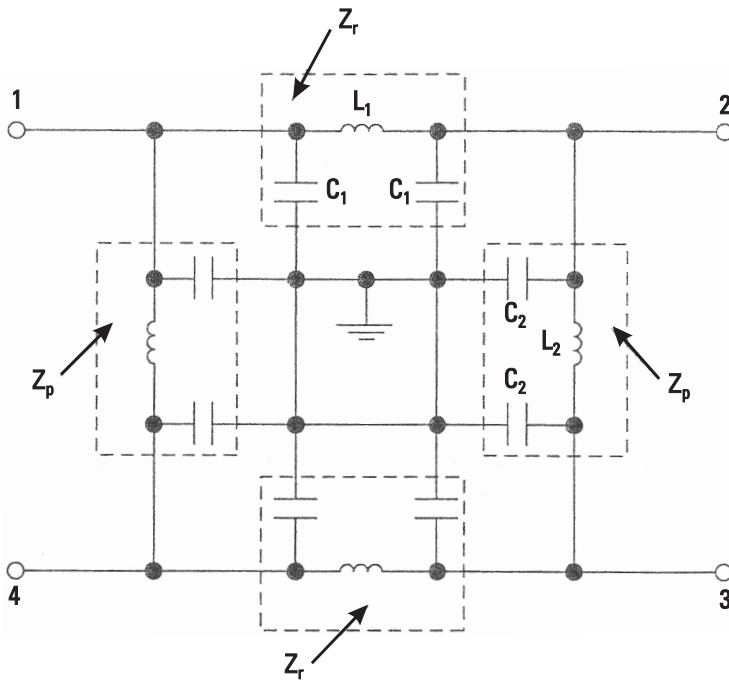


Figure 12.8 Lumped-element EC model for the 90° hybrid shown in Figure 12.7.

The $ABCD$ -matrix of any of the pi networks shown in Figure 12.8 is given by

$$\begin{aligned} \begin{pmatrix} A & B \\ C & D \end{pmatrix} &= \begin{bmatrix} 1 & 0 \\ j\omega C_1 & 1 \end{bmatrix} \begin{bmatrix} 1 & j\omega L_1 \\ 0 & 1 \end{bmatrix} \begin{bmatrix} 1 & 0 \\ j\omega C_1 & 1 \end{bmatrix} \\ &= \begin{bmatrix} 1 - \omega^2 L_1 C_1 & j\omega L_1 \\ j\omega C_1 (2 - \omega^2 L_1 C_1) & 1 - \omega^2 L_1 C_1 \end{bmatrix} \end{aligned} \quad (12.5)$$

Equating the matrix elements in (12.4) and (12.5), we get

$$\cos \theta = 1 - \omega^2 L_1 C_1, \quad \theta = \cos^{-1} (1 - \omega^2 L_1 C_1) \quad (12.6a)$$

$$Z_r \sin \theta = \omega L_1 \quad (12.6b)$$

$$\frac{1}{Z_r} \sin \theta = \omega C_1 (2 - \omega^2 L_1 C_1) \quad (12.6c)$$

$$\frac{1}{Z_r} = \sqrt{\frac{2C_1}{L_1} - (\omega C_1)^2} \quad (12.6d)$$

or

$$L_1 = \frac{Z_r \sin \theta}{\omega} \quad (12.7a)$$

$$C_1 = \frac{1}{\omega Z_r} \sqrt{\frac{1 - \cos \theta}{1 + \cos \theta}} \quad (12.7b)$$

Similarly, for the shunt line,

$$L_2 = \frac{Z_p \sin \theta}{\omega} \quad (12.8a)$$

$$C_2 = \frac{1}{\omega Z_p} \sqrt{\frac{1 - \cos \theta}{1 + \cos \theta}} \quad (12.8b)$$

When $\theta = 90^\circ$, element values become

$$L_1 = \frac{Z_r}{\omega}, \quad L_2 = \frac{Z_p}{\omega}, \quad C_t = C_1 + C_2 = \frac{1}{\omega} \left(\frac{1}{Z_r} + \frac{1}{Z_p} \right) \quad (12.8c)$$

The analysis just presented does not include losses and other lumped-element parasitic effects. Typical lumped-element values for a 900-MHz coupler designed for 50- Ω terminal impedance are $L_1 = 6.3$ nH, $L_2 = 8.8$ nH, and $C_t = 8.5$ pF. Over 900 ± 45 MHz the calculated value of amplitude unbalance and the phase difference between the output ports are ± 0.2 dB and $90 \pm 2^\circ$, respectively. Lumped-element quadrature hybrids with low insertion loss and wide bandwidth have been developed using a micromachining process [24].

12.1.2.3 Rat-Race Hybrid

Rat-race hybrid couplers, like 90° hybrids, use directly connected circuit elements and can be realized either using a distributed approach or lumped elements. Both techniques are briefly discussed next.

The rat-race hybrid is a special kind of branch-line coupler in which the circumference is an odd multiple of 1.5λ . As a result, the phase difference between the two outputs is 180° . The simplest version of this circuit is shown in Figure 12.9. Ports 1–2, 2–3, and 3–4 are separated by 90° , and port 1 and port 4 are three-quarter wavelengths away from each other. Because the characteristic impedance of each line is Z_0 and in the ring is $\sqrt{2}Z_0$, and the phase relationships shown in the structure, any power fed into port 3 splits equally into two parts that add up in phase at ports 2 and 4, and out of phase at port 1. As a result, port 1 is isolated from the input. Similarly, power fed at port 1 divides equally between ports 2 and 4 with 180° phase difference, and port 3 remains isolated.

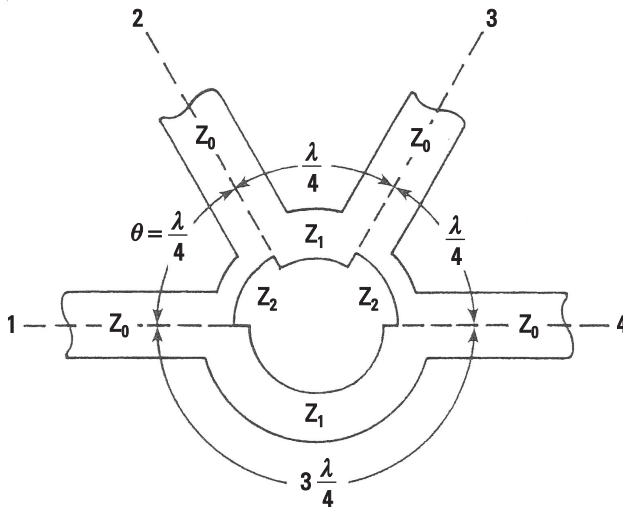


Figure 12.9 Rat-race hybrid configuration.

At the center frequency, the scattering parameters for a matched, lossless hybrid in terms of Z_1 and Z_2 (Figure 12.9) are given by

$$S_{21} = -j \frac{Z_0}{Z_2} \quad (12.9a)$$

$$S_{41} = j \frac{Z_0}{Z_1} \quad (12.9b)$$

$$S_{31} = 0 \quad (12.9c)$$

$$|S_{21}|^2 + |S_{41}|^2 = 1 \quad (12.9d)$$

The rat-race hybrid has a bandwidth (>20%) wider than that of a 90° hybrid.

The design of a lumped-element rat-race hybrid is similar to that of the lumped-element 90° hybrid described in the previous section. A lumped-element EC model for the 180° hybrid is shown in Figure 12.10. Three 90° sections are replaced by lowpass pi networks and the 270° (or -90°) section is replaced by an equivalent highpass tee network [25]. Following the same procedure as described for the 90° hybrid, the lumped elements for the pi section can be expressed as follows:

$$L_1 = \frac{\sqrt{2} Z_0 \sin \theta}{\omega} \quad (12.10a)$$

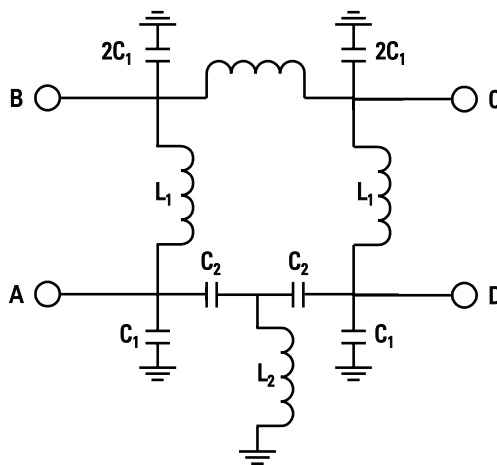


Figure 12.10 The lumped-element EC model for the 180° hybrid.

$$C_1 = \frac{1}{\sqrt{2}Z_0\omega} \sqrt{\frac{1 - \cos \theta}{1 + \cos \theta}} \quad (12.10b)$$

For the tee network, the $ABCD$ -matrix is given by

$$\begin{aligned} \begin{bmatrix} A & B \\ C & D \end{bmatrix} &= \begin{bmatrix} 1 & \frac{-j}{\omega C_2} \\ 0 & 1 \end{bmatrix} \begin{bmatrix} 1 & 0 \\ \frac{-j}{\omega L_2} & 1 \end{bmatrix} \begin{bmatrix} 1 & \frac{-j}{\omega C_2} \\ 0 & 1 \end{bmatrix} \\ &= \begin{bmatrix} 1 - \frac{1}{\omega^2 L_2 C_2} & \frac{-j}{\omega C_2} \left(2 - \frac{1}{\omega^2 L_2 C_2} \right) \\ \frac{-j}{\omega L_2} & 1 - \frac{1}{\omega^2 L_2 C_2} \end{bmatrix} \end{aligned} \quad (12.11)$$

Equating the matrix elements in (12.4) and (12.11), and using $Z_r = \sqrt{2}Z_0$,

$$L_2 = \frac{-\sqrt{2}Z_0}{\omega \sin \theta} \quad (12.12a)$$

$$C_2 = \frac{1}{\sqrt{2}Z_0\omega} \sqrt{\frac{1 + \cos \theta}{1 - \cos \theta}} \quad (12.12b)$$

when $\theta = 270^\circ$ or -90° , element values for a $50\text{-}\Omega$ system become $L_1 = L_2 = 11.25/f$ nH, and $C_1 = C_2 = 2.25/f$ pF, where f is the center frequency in gigahertz.

12.1.2.4 Directional Couplers

When two unshielded transmission lines as shown in Figure 12.11 are placed in proximity to each other, a fraction of the power present on the main line is coupled to the secondary line. The power coupled is a function of the physical dimensions of the structure, the frequency of operation, and the direction of propagation of the primary power. In these structures, continuous coupling is realized between the electromagnetic fields of the two lines, also known as parasitic coupling. If the coupled lines are of the TEM type (striplines), the power coupled to port 2 is through a backward wave, and the structure is called a *backward-wave directional coupler*. In such couplers ports 2, 3, and 4 are known as coupled, isolated, and direct ports, respectively. The phase difference between ports 1 and 2 and between ports 1 and 4 are 0 and 90° , respectively.

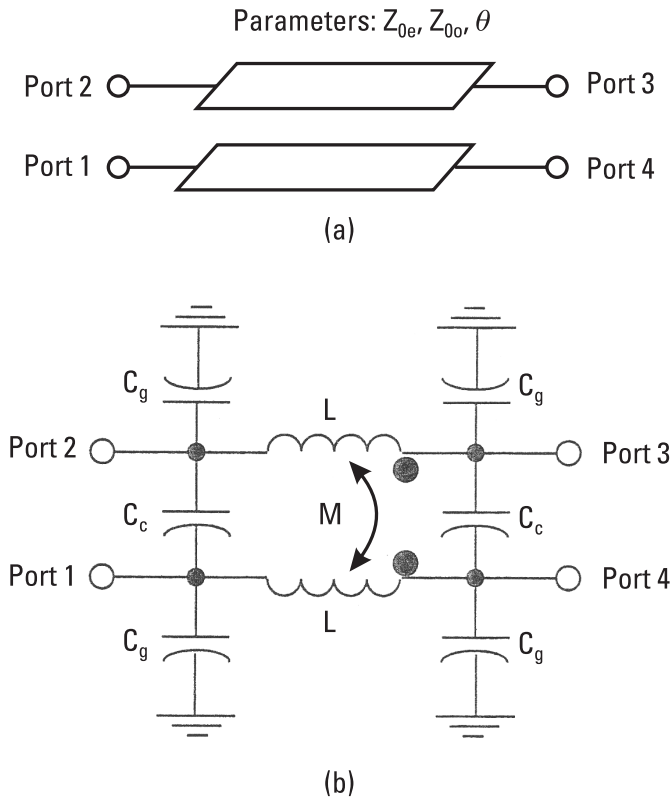


Figure 12.11 (a) Two-conductor microstrip coupled transmission lines and (b) lumped-element model.

The design equations for the TEM coupler shown in Figure 12.11(a) are summarized in the following at the center frequency of the band:

$$\theta_c = \theta_e = \theta_o = \pi/2, \quad Z_0^2 = Z_{0e} Z_{0o} \quad (12.13a)$$

$$C = -20 \log \left| \frac{Z_{0e} - Z_{0o}}{Z_{0e} + Z_{0o}} \right| \quad \text{dB} \quad (12.13b)$$

$$Z_{0e} = Z_0 \left(\frac{1 + 10^{-C/20}}{1 - 10^{-C/20}} \right)^{1/2} \quad (12.14a)$$

$$Z_{0o} = Z_0 \left(\frac{1 - 10^{-C/20}}{1 + 10^{-C/20}} \right)^{1/2} \quad (12.14b)$$

where subscripts e and o denote even and odd mode, C is the coupling coefficient expressed in decibels with positive sign, and Z_0 is the terminating impedance. To maximize the effective usable bandwidth, it is often desirable to overcouple at the design frequency, thus permitting a plus and minus tolerance across the frequency range.

Several existing coupler configurations have been transformed into new layouts to meet size target values. Some of these new configurations such as lumped-element couplers [26] and spiral directional couplers [27] are briefly described next.

12.1.2.5 Lumped-Element Couplers

The coupler shown in Figure 12.11(a) can be modeled as a lumped-element EC as shown in Figure 12.11(b). The values for L , M , C_g , and C_c in terms of Z_{0e} , Z_{0o} , and θ are obtained as follows [26]:

$$L = \frac{(Z_{0e} + Z_{0o}) \sin \theta}{4\pi f_0}, \quad C_g = \frac{\tan(\theta/2)}{Z_{0e} 2\pi f_0} \quad (12.15a)$$

$$M = \frac{(Z_{0e} - Z_{0o}) \sin \theta}{4\pi f_0}, \quad C_c = \left(\frac{1}{Z_{0o}} - \frac{1}{Z_{0e}} \right) \frac{\tan(\theta/2)}{4\pi f_0} \quad (12.15b)$$

where f_0 is the center frequency and $\theta = 90^\circ$ at f_0 . For a given coupling, using (12.14), the values of Z_{0e} and Z_{0o} are determined and then lumped-element values are calculated using (12.15). The self and mutual inductors are realized using a spiral inductor transformer, and the capacitors C_g and C_c are of the MIM type and their partial values are also included in the transformer's parasitics.

12.1.2.6 Spiral Directional Couplers

To obtain a small-size directional coupler with tight coupling, a coupled structure in the spiral shape (also known as a *spiral coupler*) is realized. Printing the spiral conductor on high dielectric constant materials further reduces the size of the coupler. In this case tight coupling is achieved by using loosely coupled parallel-coupled microstrip lines placed in proximity with the spiral configuration. This structure, as shown in Figure 12.12, uses two turns and resembles a multiconductor structure. Design details of such couplers and their modifications are given in [27], and are briefly summarized here. However, accurate design of such structures is only possible by using EM simulators.

As reported in [27], the total length of the coupled line, on the alumina substrate, along its track is $\lambda_0/8$, where λ_0 is the free-space wavelength at the center frequency and $D \cong \lambda_0/64 + 4W + 4.5S$. Parameters D , W , and S are shown in Figure 12.12. Longer lengths result in tighter couplings. The typical line width W and spacing S are approximately 500 and 40 μm , respectively,

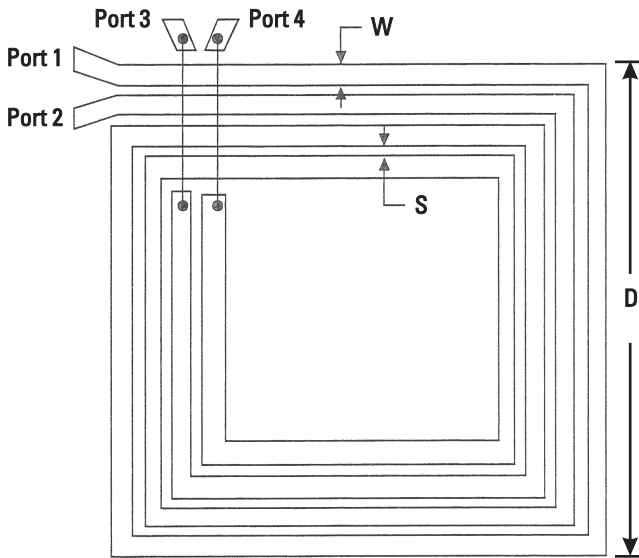


Figure 12.12 Top conductor layout of a two-turn spiral coupler.

for a 0.635-mm-thick alumina ($\epsilon_r = 9.6$) substrate. In the spiral configuration, coupling is not a strong function of spacing between the conductors. The conductors were about $5 \mu\text{m}$ thick. Measured coupled power, direct power, return loss, and isolation for the two-turn spiral coupler were approximately -3.5 , -3.5 , 22 , and 18 dB, respectively.

12.1.2.7 Transformer Directional Couplers

Simple and inexpensive broadband RF directional couplers are based on coil transformers [28–30]. Figure 12.13 shows the schematic of a directional coupler in which two identical transformers wound on magnetically isolated cores are used. The primary and secondary inductances of each transformer are denoted by L_1 and L_2 , respectively. Ports A, B, C, and D are referred to as input,

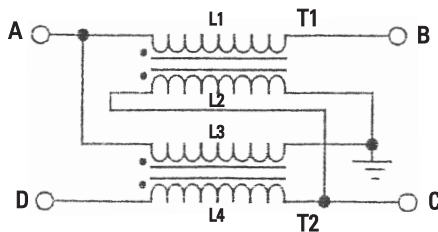


Figure 12.13 Broadband RF directional coupler schematic.

coupled, isolated, and direct ports, respectively. The analysis of such a coupler can be carried out by using its equivalent circuit, as shown in Figure 12.14, in which ports A, B, C, and D are terminated in $Z_0, Z_b, Z_c,$ and $Z_d,$ respectively. The inductive coupling between the primary and secondary is represented by $M = k\sqrt{L_1L_2}$, where k is the coupling coefficient as discussed in Chapter 11. The expressions for coupling coefficients are derived using the Kirchhoff's voltage loop equations:

$$\text{Loop 1: } -V_{in} + I_1(Z_0 + Z_b + j\omega L_1) + I_2Z_0 + I_3j\omega M = 0 \tag{12.16a}$$

$$\text{Loop 2: } -V_{in} + I_1Z_0 + I_2(Z_0 + j\omega L_2) - I_4j\omega M = 0 \tag{12.16b}$$

$$\text{Loop 3: } I_1j\omega M + I_3(Z_c + j\omega L_2) + I_4Z_c = 0 \tag{12.16c}$$

$$\text{Loop 4: } -I_2j\omega M + I_3Z_c + I_4(Z_d + Z_c + j\omega L_1) = 0 \tag{12.16d}$$

By solving the preceding equations for $Z_b = Z_c = Z_d = Z_0,$ we obtain

$$I_a = I_1 + I_2 = \left(\frac{V_{in}}{Z_0}\right) \left(\frac{L_1 + L_2}{L_1 + 2L_2}\right) \tag{12.17a}$$

$$I_b = I_1 = \left(\frac{V_{in}}{Z_0}\right) \left(\frac{L_2}{L_1 + 2L_2}\right) \tag{12.17b}$$

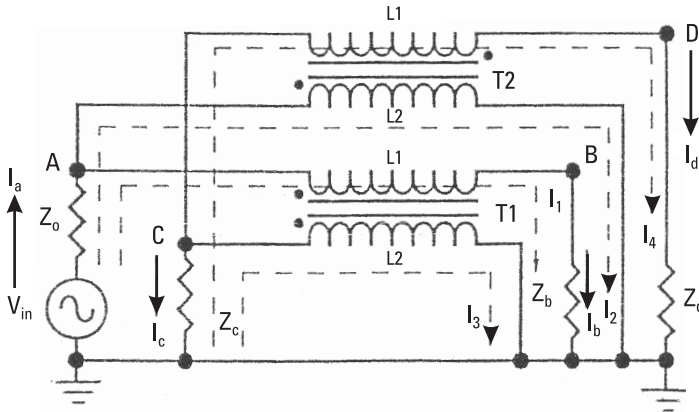


Figure 12.14 Equivalent circuit of the broadband directional coupler.

$$I_c = -(I_3 + I_4) = 0 \quad (12.17c)$$

$$I_d = I_4 = \left(\frac{V_{\text{in}}}{Z_0} \right) \left(\frac{M}{L_1 + 2L_2} \right) \quad (12.17d)$$

Voltage at each port can be written as

$$V_a = Z_0 I_a - V_{\text{in}} = \frac{V_{\text{in}} L_2}{L_1 + 2L_2} \quad (12.18a)$$

$$V_b = \frac{V_{\text{in}} L_2}{L_1 + 2L_2} \quad (12.18b)$$

$$V_c = 0 \quad (12.18c)$$

$$V_d = \frac{V_{\text{in}} M}{L_1 + 2L_2} \quad (12.18d)$$

Impedances looking into the three ports are given by

$$Z_a = \frac{V_a}{I_a} = Z_0 \left(\frac{L_2}{L_1 + L_2} \right) \quad (12.19a)$$

$$Z_b = \frac{V_b}{I_b} = Z_0 \quad (12.19b)$$

$$Z_d = \frac{V_d}{I_d} = Z_0 \quad (12.19c)$$

The preceding equations show that except for the input port, all other ports are matched. The reflection coefficient at the input is given by

$$\rho = \frac{Z_0 - Z_a}{Z_0 + Z_a} = \frac{L_1}{L_1 + 2L_2} \quad (12.20)$$

Therefore, for the input port to be matched, $L_2 \gg L_1$. When $L_1 = L_2$, ρ is 0.33 (VSWR = 2:1).

The power levels at various ports are given by:

$$P_a = V_a I_a = \left(\frac{V_{\text{in}}^2}{Z_0} \right) L_2 \left(\frac{L_1 + L_2}{(L_1 + 2L_2)^2} \right) \quad (12.21a)$$

$$P_b = \frac{V_b^2}{Z_0} = \left(\frac{V_{in}^2}{Z_0} \right) \left(\frac{L_2^2}{(L_1 + 2L_2)^2} \right) \quad (12.21b)$$

$$P_c = 0 \quad (12.21c)$$

$$P_d = \frac{V_d^2}{Z_0} = \left(\frac{V_{in}^2}{Z_0} \right) \left(\frac{L_1 L_2}{(L_1 + 2L_2)^2} \right) \quad (12.21d)$$

The relative coupled and direct power levels with respect to P_a are expressed as

$$P_{ba} = \frac{L_2}{L_1 + L_2} \quad (12.22a)$$

$$P_{da} = \frac{L_1}{L_1 + L_2} \quad (12.22b)$$

Table 12.1 summarizes the performance for various coupling coefficients for transformer directional couplers. Figure 12.15 shows a typical construction for a transformer directional coupler. Toroidal-based couplers have an operating frequency up to 1 GHz and bandwidths up to two decades [28].

12.1.3 Power Dividers/Combiners

Power dividers are commonly used in power amplifiers, mixers, active circulators, measurement systems, and phased-array antennas. In this section we discuss

Table 12.1
Simulated Performance for Various Transformer Directional Couplers

Turn Ratio N	L_2/L_1	Z_a/Z_0	P_{ba} (dB)	P_{da} (dB)	Input VSWR
1	1	0.500	-3.01	-3.01	2.00:1
2	4	0.800	-0.97	-6.99	1.25:1
3	9	0.900	-0.46	-10.00	1.11:1
4	16	0.940	-0.26	-12.30	1.06:1
5	25	0.960	-0.17	-14.10	1.04:1
6	36	0.973	-0.12	-15.70	1.03:1
8	64	0.984	-0.07	-18.30	1.02:1
10	100	0.990	-0.04	-20.00	1.01:1
12	144	0.993	-0.03	-21.60	1.01:1
15	225	0.996	-0.02	-23.50	1.00:1

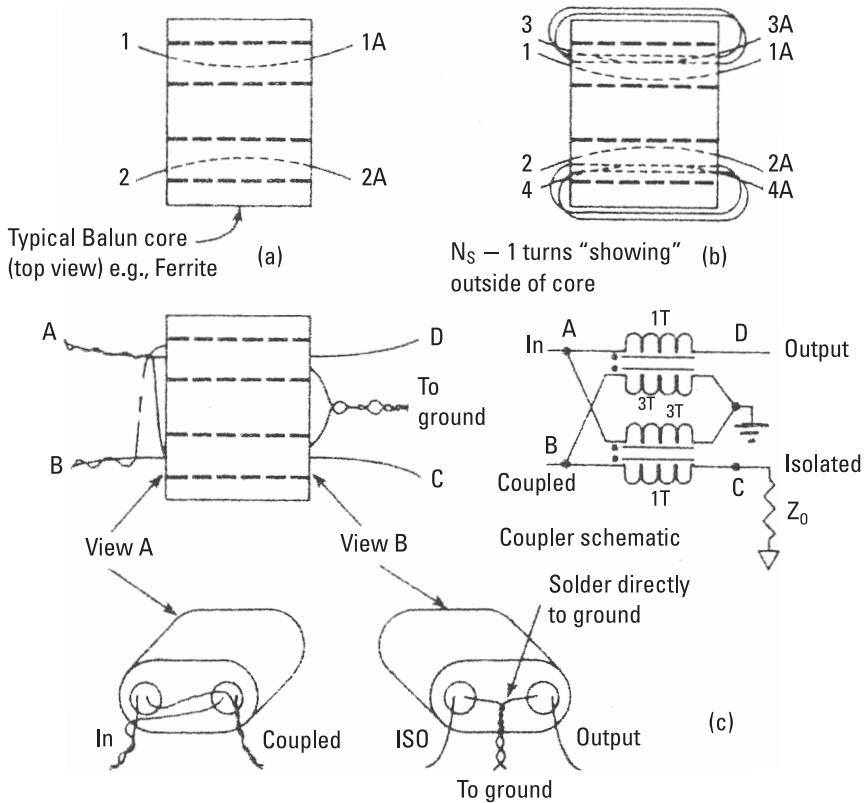


Figure 12.15 (a–c) Typical winding of a broadband 10-dB RF coupler. The number of turns in the primary and secondary are one and three, respectively.

three-port power splitters/combiners, among which the Wilkinson power divider is the most popular. A Wilkinson power divider [31, 32], also known as a two-way power splitter, offers broad bandwidth and equal phase characteristics at each of its output ports. Figure 12.16 shows its schematic diagram. The isolation between the output port is obtained by terminating the output ports by a series resistor. Each of the quarter-wave lines shown in Figure 12.16 has the characteristic impedance of $\sqrt{2}Z_0$ and the termination resistor has the value of $2Z_0 \Omega$, Z_0 being the system impedance. A Wilkinson power divider offers a bandwidth of about one octave. The performance of this divider can be further improved, depending on the availability of space, by the addition of a $\lambda/4$ transformer in front of the power-division step. The use of multisections makes it possible to obtain a decade bandwidth. These power dividers can be designed to be unequal power splitters by modifying the characteristic impedances of the $\lambda/4$ sections and isolation resistor values [4, 8].

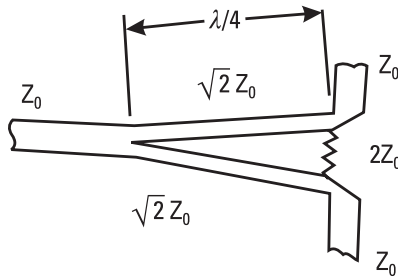


Figure 12.16 Wilkinson divider configuration.

The design of lumped-element power dividers [33, 34] is similar to 90° and 180° hybrids; that is, the $\lambda/4$ sections are replaced by equivalent LC networks. Figure 12.17 shows a lumped-element version of a two-way power divider using pi equivalent lowpass LC networks.

Table 12.2 summarizes the values of LC elements for the pi and tee equivalent lowpass and highpass LC networks. Here $Z_r = \sqrt{2}Z_0$ and $\theta = \pi/2$. Typical lumped-element values for a divider shown in Figure 12.17 designed at 1 GHz for 50Ω terminal impedance are $L = 11.25$ nH, $C = 2.25$ pF, and $R = 100\Omega$. Again the simple equations included in Table 12.2 do not include losses and parasitic effects.

12.1.4 Matching Networks

Matching networks for RF and microwave circuits are generally designed to provide a specified electrical performance over the required bandwidth. To realize compact circuits, lumped-element matching networks are utilized to transform the device impedance to 50Ω . At RF frequencies lumped discrete

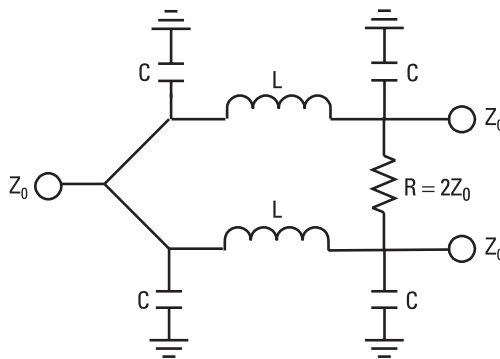
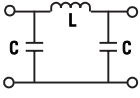
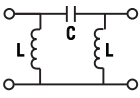
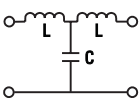
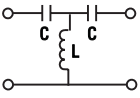


Figure 12.17 Lumped-element EC model for the two-way power divider.

Table 12.2
LC Element Values of Several Networks

Configuration	Element Values
"pi" lowpass 	$L = \frac{\sqrt{2}Z_0 \sin \theta}{\omega}$ $C = \frac{1}{\sqrt{2}Z_0 \omega} \sqrt{\frac{1 - \cos \theta}{1 + \cos \theta}}$
"pi" highpass 	$L = \frac{\sqrt{2}Z_0}{\omega} \sqrt{\frac{1 + \cos \theta}{1 - \cos \theta}}$ $C = \frac{1}{\sqrt{2}Z_0 \omega \sin \theta}$
"tee" lowpass 	$L = \frac{\sqrt{2}Z_0}{\omega} \sqrt{\frac{1 - \cos \theta}{1 + \cos \theta}}$ $C = \frac{\sin \theta}{\omega \sqrt{2}Z_0}$
"tee" highpass 	$L = \frac{\sqrt{2}Z_0}{\omega \sin \theta}$ $C = \frac{1}{\sqrt{2}Z_0 \omega} \sqrt{\frac{1 + \cos \theta}{1 - \cos \theta}}$

spiral inductors, MIM capacitors, and thin-film resistors are primarily used in matching networks. Lumped-element circuits that have lower Q than distributed circuits have the advantage of smaller size, lower cost, and wide bandwidth characteristics. These are especially suitable for MMICs and for broadband hybrid MICs in which "real estate" requirements are of prime importance. Impedance transformations on the order of 20:1 can be easily accomplished using the lumped-element approach. Therefore, high-power devices that have very low impedance values can easily be tuned with large impedance transformers realized using lumped elements. At low frequencies (below C-band), MMICs designed using lumped inductors and capacitors have an order of magnitude smaller die size compared to ICs designed using distributed matching elements such as microstrip lines.

Lowpass matching networks in amplifiers provide good rejection for high-frequency spurious and harmonic frequencies but have a tendency toward high

gain (and, hence, instability) at very low frequencies. Thus, in multistage amplifiers, a combination of bandpass at the input stage and interstages and lowpass at the output stage will produce the required frequency response. This section describes various LC configurations suitable for designing matching networks.

An impedance can be represented by a parallel combination of a resistance and a reactance or an equivalent series combination of a resistance and reactance as shown in Figure 12.18. Thus, one can convert a parallel network to an equivalent series network using the following relations:

$$R_S = R_P X_P^2 / (R_P^2 + X_P^2) \quad (12.23a)$$

$$X_S = X_P R_P^2 / (R_P^2 + X_P^2) \quad (12.23b)$$

Similarly, a series network can be converted into a parallel network using the following equations:

$$R_P = (R_S^2 + X_S^2) / R_S \quad (12.24a)$$

$$X_P = (R_S^2 + X_S^2) / X_S \quad (12.24b)$$

12.1.4.1 L-Network

Inductors and capacitors connected in an L-section configuration are widely used as impedance-matching circuit elements. As shown in Figure 12.19, eight possible arrangements of inductors and capacitors can be utilized. The range

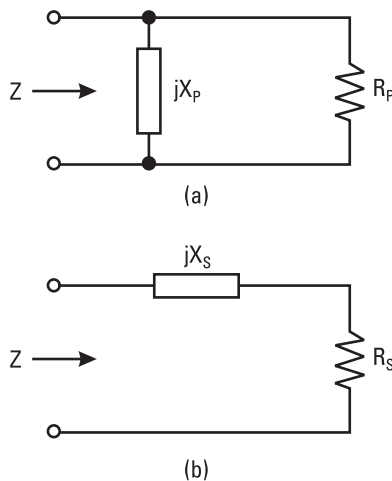


Figure 12.18 (a) Parallel and (b) series representations of an impedance.

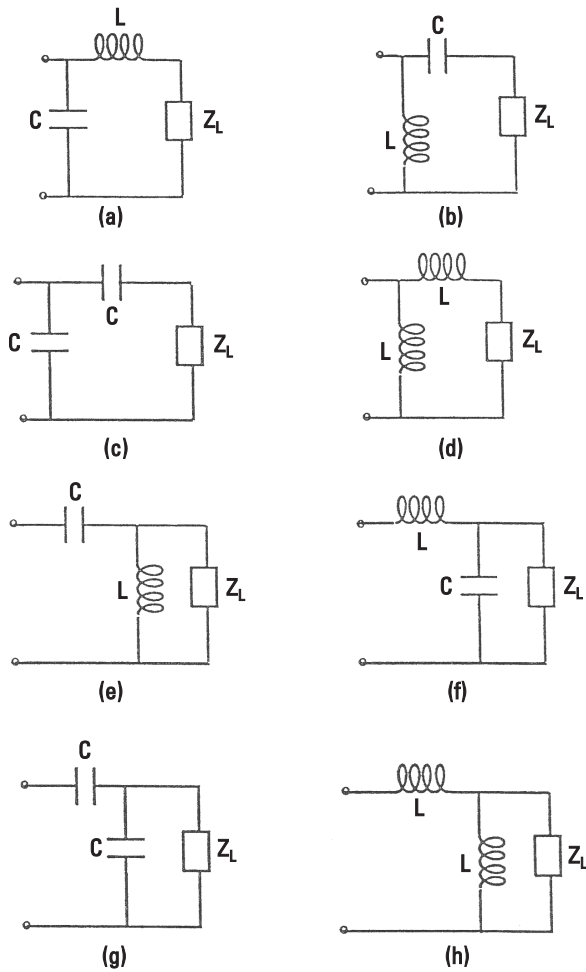


Figure 12.19 (a–h) Eight topologies of lumped-element matching networks.

of impedance transformation depends on the value of the original inductors or capacitors in the L-configuration. Rearranging (12.24a), we get

$$\frac{R_P}{R_S} = 1 + Q^2, \quad \text{where } Q = X_S/R_S \quad (12.25)$$

When a reactance X_S is added in series with a resistor R_S , and converted to an equivalent parallel combination, the resistance increases by a $1 + Q^2$ factor. Conversely, when a reactance X_P is added in parallel with a resistor R_P , and converted to an equivalent series combination, the resistance decreases.

These properties of network conversion are used to design L-section matching networks.

Two basic topologies of L-section matching networks are shown in Figure 12.20. These networks consist of purely reactive elements. The impedances Z_{SE} and Z_{SH} of the series (reactance) and shunt (susceptance) elements are represented by jX and jB , respectively. Consider a design problem where the complex load impedance $Z_L (= R_L + jX_L)$ is required to be transformed to a real impedance $Z_{IN} (= Z_0)$.

When $R_L < Z_0$, the configuration in Figure 12.20(a) is used and

$$Z_{in} = Z_0 = \left[jB + \frac{1}{R_L + j(X + X_L)} \right]^{-1} \quad (12.26)$$

By equating real and imaginary parts,

$$X = \pm \sqrt{R_L(Z_0 - R_L)} - X_L \quad (12.27a)$$

$$B = \pm \frac{\sqrt{(Z_0 - R_L)/R_L}}{Z_0} \quad (12.27b)$$

The positive and negative signs imply that there are two possible solutions. Positive reactance corresponds to an inductor and negative reactance implies a capacitor. Similarly, a positive susceptance corresponds to a capacitor and a negative susceptance implies an inductor.

If $R_L > Z_0$, the configuration in Figure 12.20(b) is used and

$$Z_{in} = Z_0 = jX + \frac{1}{jB + (R_L + jX_L)^{-1}} \quad (12.28)$$

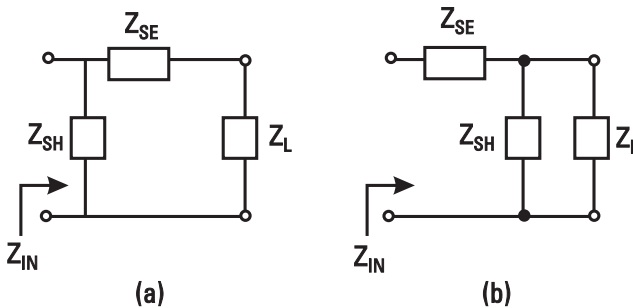


Figure 12.20 (a, b) Two basic configurations of L-shaped lumped-element matching networks.

Again, by equating real and imaginary parts,

$$B = \frac{X_L \pm \sqrt{R_L/Z_0} \sqrt{R_L^2 + X_L^2 - Z_0 R_L}}{R_L^2 + X_L^2} \quad (12.29a)$$

$$X = \frac{1}{B} + \frac{X_L Z_0}{R_L} - \frac{Z_0}{B R_L} \quad (12.29b)$$

Again, there are two possible solutions. Once the values of X and B are determined, one could proceed to calculate the values of the lumped elements needed at the design frequency.

12.1.4.2 Tee and Pi Networks

To get a larger bandwidth and realize large impedance ratios, more elements are required in the matching networks. The tee and pi arrangements of lumped elements, shown in Figure 12.21, are commonly used. Such arrangements are simply considered back-to-back L-section networks. The addition of one more element to the simple L-section matching circuit gives the designer much greater control over the bandwidth and also permits the use of more practical circuit elements. The circuit configurations and circuit element values [35] are given in Figure 12.21 where

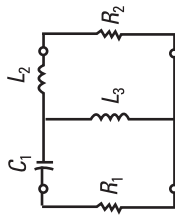
$$M = \frac{R_2}{R_1} > 1 \quad \text{and} \quad N > M \quad (12.30)$$

and where M is the impedance transformation ratio and N is a variable. By properly selecting N , a compromise is obtained in terms of bandwidth and realizable circuit element values. For more details the readers are referred to recently published books [36, 37].

12.1.5 Lumped-Element Biasing Circuit

Solid-state devices require low frequency and dc bias circuitry that must be separated from the RF circuit. In other words, when a bias voltage is applied to the device, the RF energy should not leak through the bias port. In practice, many biasing circuits are used [20]. Lumped-element biasing circuits are described in this section. The circuit performance is discussed by calculating the VSWR response of these circuits. The desirable features of these biasing circuits are small RF leakage and broad bandwidth characteristics.

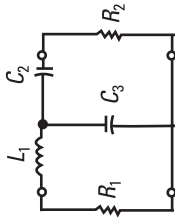
A shunt coil inductor, L , also known as an RF choke, is used as a biasing element while a series capacitor C is used to isolate the bias voltage applied to



$$C_1 = \left(\omega_0 R_1 \sqrt{N-1} \right)^{-1}$$

$$L_2 = R_2 \frac{\sqrt{\frac{N}{M}-1}}{\omega_0}$$

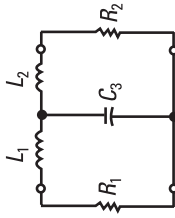
$$L_3 = \frac{NR_1}{\omega_0 \left(\sqrt{N-1} - \sqrt{\frac{N}{M}-1} \right)} \quad (d)$$



$$L_1 = R_1 \frac{\sqrt{N-1}}{\omega_0}$$

$$C_2 = \left(\omega_0 R_2 \sqrt{\frac{N}{M}-1} \right)^{-1}$$

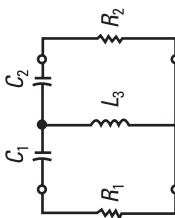
$$C_3 = \frac{\sqrt{N-1} + \sqrt{\frac{N}{M}-1}}{\omega_0 NR_1} \quad (c)$$



$$L_1 = R_1 \frac{\sqrt{N-1}}{\omega_0}$$

$$L_2 = R_2 \frac{\sqrt{\frac{N}{M}-1}}{\omega_0}$$

$$C_3 = \frac{\sqrt{N-1} + \sqrt{\frac{N}{M}-1}}{\omega_0 NR_1} \quad (b)$$



$$C_1 = \left(\omega_0 R_1 \sqrt{N-1} \right)^{-1}$$

$$C_2 = \left(\omega_0 R_2 \sqrt{\frac{N}{M}-1} \right)^{-1}$$

$$L_3 = \frac{NR_1}{\omega_0 \left(\sqrt{N-1} + \sqrt{\frac{N}{M}-1} \right)} \quad (a)$$

Figure 12.21 (a-d) T-section matching configurations.

various circuits. Shunt inductor and series capacitor circuits are shown in the inset of Figure 12.22. The normalized admittance of the coil and normalized impedance of the capacitor backed by a 50-Ω matched element are given by

$$y = 1 - j \frac{Z_0}{\omega L} \tag{12.31}$$

$$z = 1 - j \frac{1}{\omega CZ_0} \tag{12.32}$$

If $y = z$, that is, $Z_0^2 = L/C$, the both elements will have an equal VSWR at all frequencies. The VSWR in each case can be written

$$\text{VSWR} = (1 + |\rho|)/(1 - |\rho|) \tag{12.33}$$

where

$$|\rho| = \frac{Z_0/\omega L}{[4 + (Z_0/\omega L)^2]^{1/2}} \text{ for a shunt coil} \tag{12.34a}$$

$$= \frac{1/\omega CZ_0}{[4 + (1/\omega CZ_0)^2]^{1/2}} \text{ for a series capacitor} \tag{12.34b}$$

The *insertion loss* (IL) of a reactive discontinuity having a VSWR, S , is given by

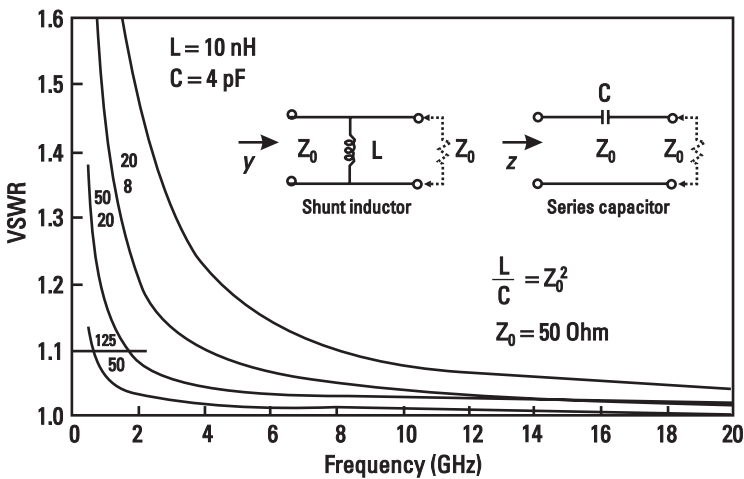


Figure 12.22 L and C biasing networks and their responses.

$$IL = 20 \log \left(\frac{S + 1}{2\sqrt{S}} \right) \quad (12.35)$$

Variation of VSWR corresponding to these elements is shown in Figure 12.22. Higher values of L or C have a lower VSWR. When both of these elements are used simultaneously, the elements should be connected at the same plane. The normalized admittance of the capacitor, which is backed by a $50\text{-}\Omega$ matched line, becomes

$$y_c = \frac{1 + j \frac{1}{\omega CZ_0}}{1 + \frac{1}{(\omega CZ_0)^2}} \quad (12.36)$$

This admittance will add to the admittance of the inductor ($y_L = -jZ_0/\omega L$). The total admittance y_t is given by

$$y_t = y_c + y_L \quad (12.37)$$

When $\omega CZ_0 \gg 1$

$$y_t = 1 + j \left(\frac{1}{\omega CZ_0} - \frac{Z_0}{\omega L} \right) \quad (12.38)$$

If $Z_0^2 = L/C$, $y_t = 1$. Thus, the VSWR will be unity and also independent of frequency as long as L and C are independent of frequency.

12.2 Control Circuits

Semiconductor control circuits, such as switches, phase shifters, attenuators, and modulators, have been used extensively in radar, communication systems, electronic warfare, wireless applications, instruments, and other systems for controlling the signal flow or to adjust the phase and amplitude of the signal. At RF, microwave, and millimeter-wave frequencies, many of the problems of bandwidth, switching speed, power handling, high dynamic range, low voltage operations, and high operating frequency have already been solved. An excellent overview of control circuits and switching devices can be found in [7, 15, 17, 38–43]. Here only switches, phase shifters, and attenuators having unique performance when designed using lumped elements are described.

12.2.1 Switches

In microwave systems, the transmitter and receiver section is called a *transceiver*. Transceivers have different requirements for switches including low and high power, narrowband and broadband, and high isolation. Lumped elements play an important role in achieving broad bandwidths, high isolation, and high power levels in RF/microwave switches. Examples of high isolation and high-power switches are discussed next.

12.2.1.1 High Isolation Switches

Several techniques are available for improving the isolation of switches, including the use of low “off” state capacitance FETs [44], distributed with tuning inductors [7, Chapter 12], and achieving band-rejection filter in the operating frequency range [45]. Basically, in these schemes either the off state capacitance of the switching device is tuned out or its effect is minimized. In all of these methods, the insertion loss of the switches more or less remains the same. Figure 12.23 shows a simplified version of a *single-pole single-throw* (SPST) switch using a band-rejection filter technique to improve the isolation in the operating frequency band. FETs 1, 2, and 3 constitute a conventional SPST switch, and the T-shaped R-C-R network is added to improve the isolation in the off state. To a first-order approximation, the element values of the R-C-R network can be calculated from the transistor’s “on” state resistance and off state capacitance using the following equations [45]:

$$f_0 = \frac{1}{2\pi\sqrt{2C_{\text{off}1} C_{\text{off}3} R_{\text{on}2} R}} \quad (12.39a)$$

$$RC = 2R_{\text{on}2} \cdot (C_{\text{off}1} + C_{\text{off}3}) \quad (12.39b)$$

where $R_{\text{on}x}$ and $C_{\text{off}x}$ are the on resistance and off capacitance of the x th switching device, respectively. Here f_0 is the center frequency of the operating band and the switch is assumed to be terminated into a $50\text{-}\Omega$ input–output impedance. With this method, the isolation was improved by more than 15 dB over about a 20% bandwidth in the C-band [45].

12.2.1.2 High-Power Switches

For several communication and radar applications, one needs high-power handling switches. The maximum power-handling capacity of switches depends on the maximum voltage that can be applied safely to the device in the off state and the maximum current limit of the FET in the on state. The maximum power, P_{max} , that can be transmitted for a shunt FET switch is given by

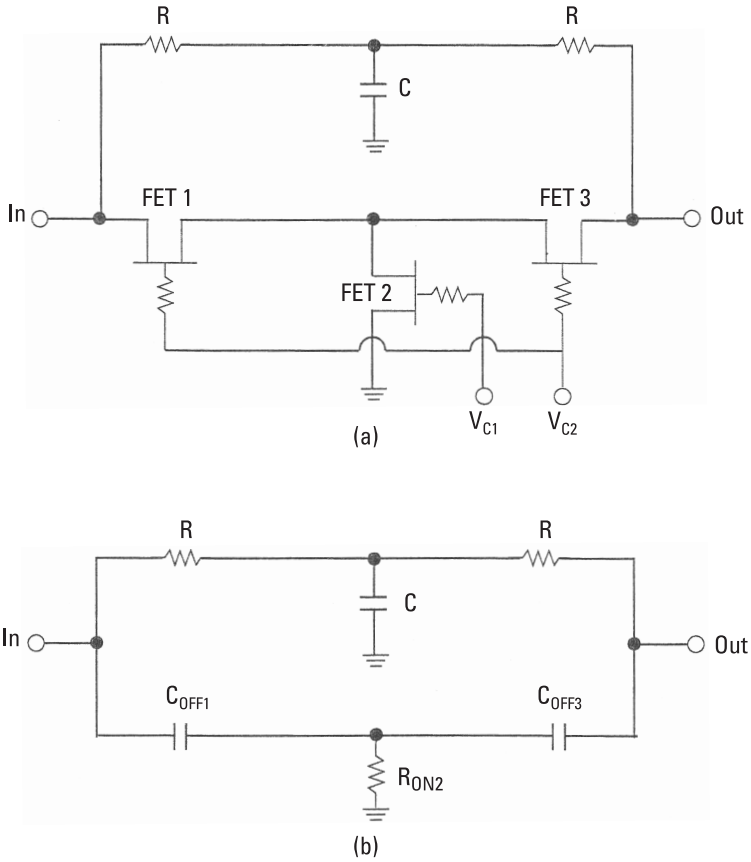


Figure 12.23 (a) Circuit configuration of the improved isolation FET switch and (b) its equivalent in the off state.

$$P_{\max} = \frac{(V_B - V_p)^2}{2Z_0} \tag{12.40}$$

For low-voltage applications, where the breakdown voltage is much greater than the control voltage V_c , the maximum power is given by

$$P_{\max} = \frac{2(V_c - V_p)^2}{Z_0} \tag{12.41}$$

where V_p is the pinch-off voltage of the device, V_B is the breakdown voltage between the gate and drain terminals, and Z_0 is the impedance level the shunt FET sees in its off state. Both V_c and V_p are positive quantities. When the

shunt FET is in the on state, there is no voltage at the gate terminal. The maximum power capacity is determined by the short-circuited current, which is equal to the maximum drain-source current (I_{dss}) of the FET or HEMT and is proportional to the gate periphery. Again, if Z_0 is the impedance level that the switch FET sees in its low impedance state, then the maximum power-handling capacity is given by

$$P_{\text{max}} = \frac{1}{2} I_{\text{dss}}^2 Z_0$$

or

$$I_{\text{dss}} = \sqrt{\frac{2P_{\text{max}}}{Z_0}} \quad (12.42)$$

Equations (12.40) and (12.42) are used to design switching FETs for high-power operation. Based on the maximum power requirements and a given breakdown voltage, the gate periphery of the FET is selected. Based on (12.40) and (12.42), available bias voltages and breakdown voltage, conventional switches can handle up to a few watts. Several methods have been discussed [43] to improve the power-handling capability of FET switches using low-power switching FETs. These techniques include (1) impedance transformation, (2) stacked FETs, and (3) LC resonant circuits. The impedance transformation technique that uses two $\lambda/4$ transformers occupy a considerably large area on GaAs chips. One can reduce the chip size by using lumped-element-based transformers; however, both impedance transformation and stacked FET techniques require FETs with large pinch-off voltages and high breakdown voltages. To overcome these limitations, a novel technique known as LC -resonant was introduced by Tokumitsu et al. [46]. This works well at low supply voltages and does not require high breakdown voltage FETs.

Figure 12.24 shows a conventional series/shunt FET *transmit/receive* (T/R) switch and LC -resonant circuit configuration. In an LC -resonant circuit switch configuration, the shunt FET (SW-a) in the transmitting path and series FET (SW-c) in the receiving path in Figure 12.24(a) are replaced with a combination of FETs and an LC -resonant circuit as shown in Figure 12.24(c). In Figure 12.24(b) each box is equivalent to an LC -resonant circuit. The LC -resonant circuit consists of spiral inductors and MIM capacitors. In Figure 12.24(c), the capacitance C_s represents the FET's total capacitance in the off state. When the FETs are in the on state, the switch between 1 and 2 is in the off state because of the parallel resonance of inductor L_1 and capacitance C_1 . Conversely, the switch between 1 and 2 is in the on state when the FETs are in the off state, due to the series resonance of inductor L_1 and C_2 shunted by C_s .

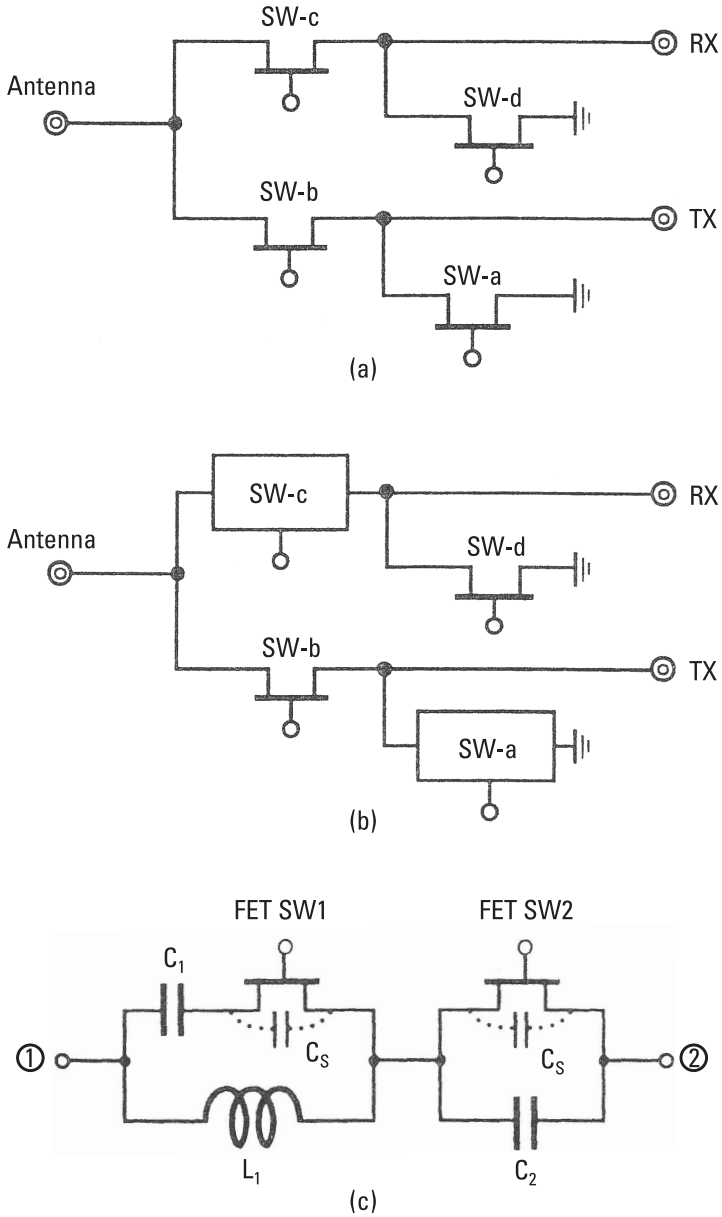


Figure 12.24 Typical T/R switch configurations for (a) conventional and (b) improved power-handling configuration; (c) SW-a/SW-c using the LC-resonant circuit technique.

Thus, in this scheme the FET switchable LC resonator uses a reverse control voltage scheme, that is, the FET switchable LC resonator is off when the FET devices are on and vice versa. Thus, this technique uses a unique scheme of biasing T/R switches—only one control line for both transmitting and receiving modes because all FETs will be on for the transmitting mode and off for the receiving mode. In the transmit mode, P_{\max} and the linearity of LC -resonant circuit-based switches can be enhanced by increasing the gate periphery of FETs.

The P_{\max} of this scheme is given by

$$P_{\max} = \frac{Z_0}{2} \left(\frac{I_{\text{dss}}}{Q_L} \right)^2 \quad (12.43)$$

where Z_0 , I_{dss} , and Q_L are the system impedance, drain-source saturation current of the FET devices, and loaded Q of the T/R switch in the transmit mode, respectively. Figure 12.25 compares P_{\max} for this scheme and stacked FET technique, where the pinch-off voltage is -1V and the control voltage is $0\text{V}/-2\text{V}$. The LC -resonant circuit technique shows great potential for high-power operation for large gate periphery FETs.

Figure 12.26 shows a T/R switch schematic and a photograph of a MMIC chip. The LC resonators are placed where a large RF voltage is applied in the transmitting mode. There is one shunt FET in the receiver arm and two series FETs in the shunt branch of the transmitting arm. All FETs have 0.48-mm gate peripheries and $0\text{V}/-2\text{V}$ as the control voltage. The design trade-offs are the FET gate periphery (W_g), FET off capacitance C_{so} (pF/mm), and the

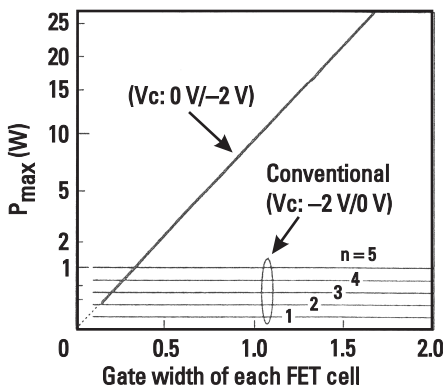


Figure 12.25 Maximum transmitting power comparison between the proposed LC -resonant T/R switch and conventional series/shunt FET T/R switches where $I_{\text{dss}} = 0.2$ A/mm, $V_p = -1\text{V}$, and $Q_L = 0.44$.

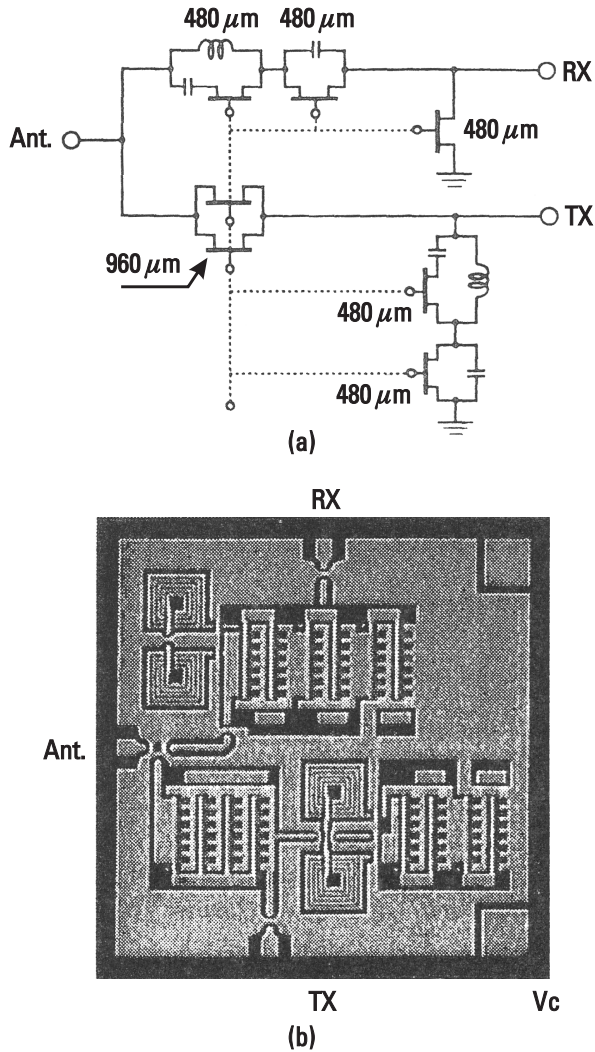


Figure 12.26 (a) Circuit topology and (b) MMIC photograph of an LC-resonant T/R switch, which measures only 2×2 mm in chip size. (From: [46]. © 1995 IEEE. Reprinted with permission.)

bandwidth balance between the transmitting and receiving arms. A simple design equation, relating these quantities, is given by [46]

$$W_{g \max} \text{ (mm)} = 1.4 [f_0 \text{ (GHz)} \cdot C_{so} \text{ (pF/mm)}]^{-1} \quad (12.44)$$

where f_0 is the center frequency of operation and the system's impedance (Z_0) is 50Ω .

Figure 12.27 shows the measured output power/tone and third *intermodulation rejection* (IMR) as a function of input power. The measured insertion loss and isolation at about 2 GHz were better than 2 and 30 dB, respectively. The measured rise/fall times characteristics were similar to those for conventional T/R switches.

12.2.2 Phase Shifters

One of the important elements in a T/R module is the programmable multibit phase shifter. The scanning of the beam in phased-array radars is achieved by changing the phase of the RF signal fed to or received from each radiating element. For beam steering, programmable bidirectional phase shifters are required to adaptively adjust the transceiver phase in both the transmitting and the receiving modes.

The four main types of solid-state digitally controlled phase shifters are switched line, reflection, loaded line, and lowpass/highpass, as shown in Figure 12.28. The first three types can be realized using both distributed and lumped elements, while the lowpass/highpass topology uses only lumped elements. The lowpass/highpass phase shifter configuration is very suitable for narrowband and broadband and compact size applications. Here the digital phase shift is realized by using the phase lag property of the lowpass network and phase lead characteristic of the highpass network, which are connected between two SPDT switches. The small bits are of an embedded-FET type, where the FET's reactances become part of the phase shifting lowpass/highpass networks.

Generally, the digital bits in a multibit phase shifter have binary values; that is, 4-bit and 5-bit phase shifters have 180° , 90° , 45° , 22.5° bits and 180° , 90° , 45° , 22.5° , 11.25° bits, respectively. Several different topologies have been

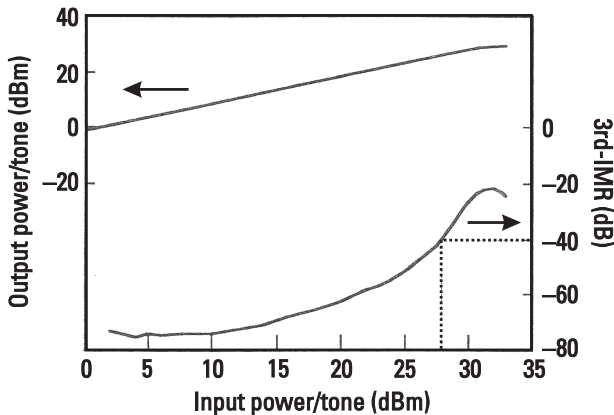


Figure 12.27 Linearity of the improved power-handling capability of an LC-resonant T/R switch.

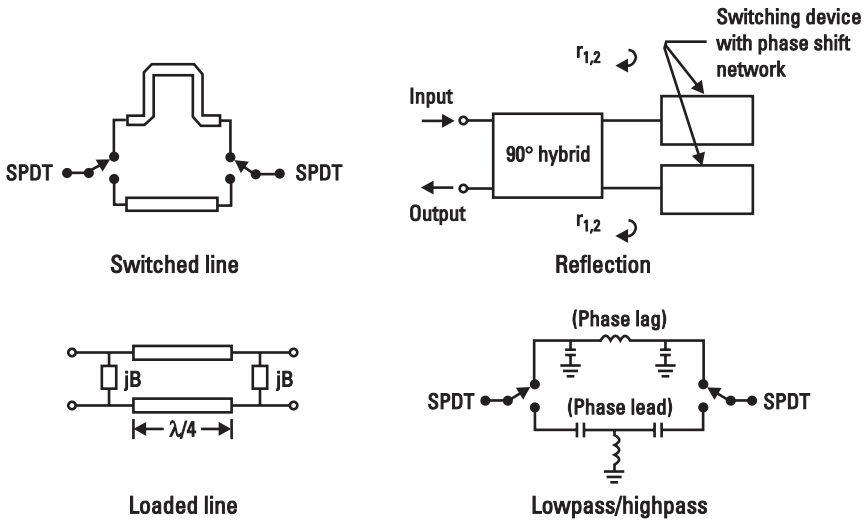


Figure 12.28 Four basic phase shifter configurations.

reported in the literature [47–51]. The 180° bit is commonly designed using a switched lowpass/highpass topology as shown in Figure 12.29(a). The simplest topology for 90° and smaller bits is shown in Figure 12.29(b).

Assuming ideal switches, for 180° bit, the values of L_1 , C_1 and L_2 , C_2 for a 50-Ω system are calculated from (12.7) and Table 12.2, respectively. These values are

$$L_1 = L_2 = \frac{50}{2\pi f}, \quad C_1 = C_2 = \frac{1}{50 \times 2\pi f} \tag{12.45}$$

The first-order equation for circuit elements for 90° and lower bits can be derived as follows: When FET 1 is in the on state, FET 2 is in the off state, and the value of L_p is selected to parallel resonate out the off-state capacitance of FET 2, the circuit is simplified to a single series on-resistance of FET 1. Thus, in the reference state, the phase shifter has an insertion loss that depends on the FET 1 size and approximately zero insertion phase. On the other hand, when FET 1 is in the off state and FET 2 is in the on state, Figure 12.29(b) is reduced to the equivalent circuit shown in Figure 12.30. Here the total capacitance C_T is given by

$$C_T = C_S + C_{\text{off1}} \tag{12.46}$$

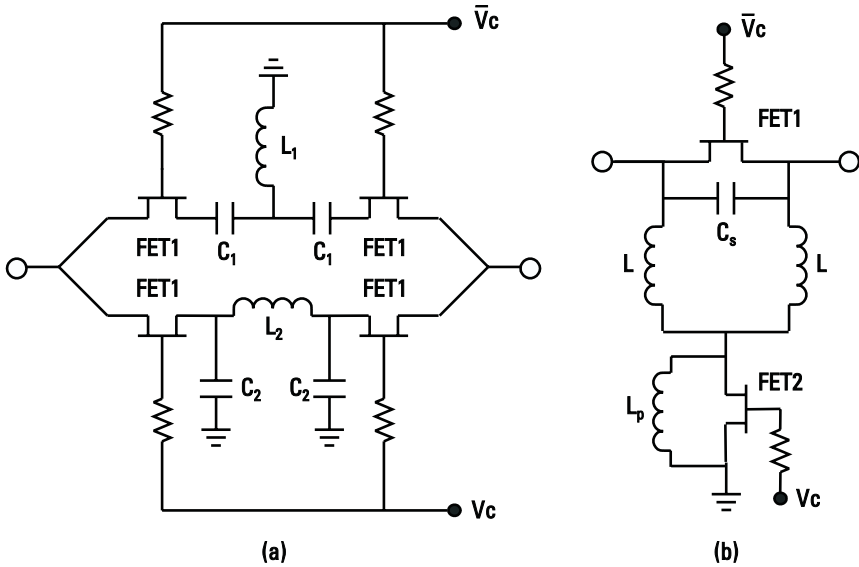


Figure 12.29 Schematics for multibit phase shifters: (a) 180° bit and (b) 90°, 45°, and 22.5° bits.

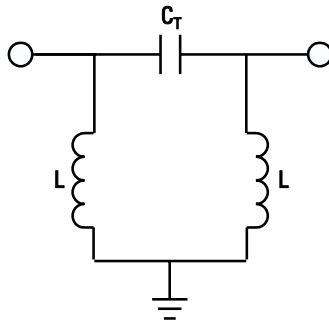


Figure 12.30 Pi LC representation.

where C_{off1} is the off-state capacitance of FET 1. When the system impedance is Z_0 and under matched conditions, the values of L and C_T using Table 12.2 can be expressed as follows:

$$L = \frac{Z_0}{\omega} \sqrt{\frac{1 + \cos \theta}{1 - \cos \theta}} = \frac{Z_0}{\omega \tan(\theta/2)} \tag{12.47}$$

$$C_T = \frac{1}{\omega Z_0 \sin \theta} \tag{12.48}$$

where θ is the insertion phase. Thus, for a given phase shift, the values of C_s and L are determined using (12.46), (12.47), and (12.48).

12.2.3 Digital Attenuator

Digital multibit attenuators offer precise attenuation ranges, good linearity, good thermal stability, and high power-handling capability. The multibit attenuators are realized using a tee attenuator topology in which the switching FETs become an integral part of the attenuator configuration. This results in compact size and low insertion loss. In a 6-bit attenuator, the small, that is, 0.5-, 1-, and 2-dB, bits are generally realized using a topology like that shown in Figure 12.31(a), whereas 4- and 8-dB bits use the topology shown in Figure 12.31(b). The 16-dB bit will basically use two 8-dB bits. The RC network shown in Figure 12.31 is optimized to maintain the attenuator's linearity and a good VSWR. The combination of thin-film resistors, active resistors, and the FET's parasitic resistance are used to set the attenuation value of each bit.

In addition to the tee configuration, pi and bridged-tee topologies, as summarized in Table 12.3, are also used.

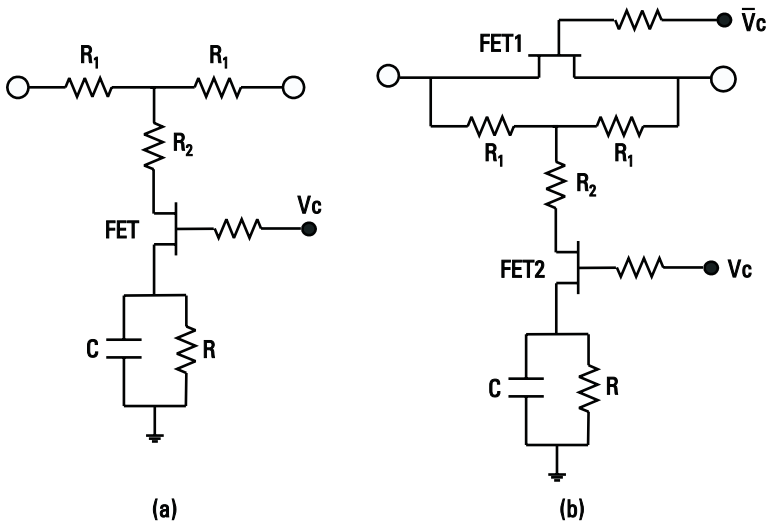
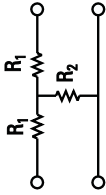
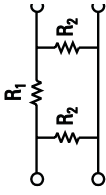
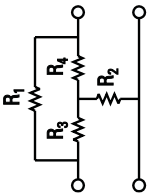


Figure 12.31 Schematic for multibit attenuators: (a) 0.5-, 1-, and 2-dB bits and (b) 4- and 8-dB bits.

Table 12.3
 Characteristics of Tee, Pi, and Bridged-tee Attenuators

	Tee	Pi	Bridged-Tee
Configuration			
Matching conditions	$Z_0^2 = R_1^2 + 2R_1R_2$	$Z_0^2 = \frac{R_2^2}{1 + 2R_2/R_1}$	$R_3 = R_4 = Z_0$ $Z_0^2 = R_1R_2$
Attenuation at matching	$A = \frac{V_0}{V_1} = \frac{R_2}{R_1 + R_2 + Z_0}$	$A = \frac{V_0}{V_1} = \frac{R_2Z_0}{R_1R_2 + Z_0(R_1 + R_2)}$	$A = \frac{R_2}{Z_0 + R_2}$ $A = \frac{Z_0}{Z_0 + R_1}$
Attenuation (dB)	R_1 (Ω)	R_1 (Ω)	R_1 (Ω)
0.5	1.4	2.9	3
1	2.9	5.8	6
3	8.5	17.6	20
5	14	31	39
10	26	71	108
15	35	136	231
	R_2 (Ω)	R_2 (Ω)	R_2 (Ω)
0.5	868	1,737	843
1	433	869	409
3	142	292	120
5	82	179	64
10	35	96	23
15	18.4	72	10.8

References

- [1] Matthaei, G. L., L. Young, and E. M. T. Jones, *Microwave Filters, Impedance-Matching Networks and Coupling Structures*, New York: McGraw-Hill, 1964.
- [2] Skwirzynski, J. K., *Design Theory and Data for Electrical Filters*, London: Van Nostrand, 1965.
- [3] Zverev, A. I., *Handbook of Filter Synthesis*, New York: John Wiley, 1967.
- [4] Howe, Jr., H., *Stripline Circuit Design*, Dedham, MA: Artech House, 1974.
- [5] Rhodes, J. D., *Theory of Electrical Filters*, New York: John Wiley, 1976.
- [6] Malherbe, J. A. G., *Microwave Transmission Line Filters*, Dedham, MA: Artech House, 1979.
- [7] Bahl, I. J., and P. Bhartia, *Microwave Solid State Circuit Design*, New York: John Wiley, 1988, Chap. 6.
- [8] Chang, K., (Ed.), *Handbook of Microwave and Optical Components*, Vol. 1, New York: John Wiley, 1989.
- [9] Rhea, R. W., *HF Filter Design and Computer Simulation*, Atlanta, GA: Noble Publishing, 1994.
- [10] Hong, J.-S., and M. J. Lancaster, *Microstrip Filters for RF/Microwave Applications*, New York: John Wiley, 2001.
- [11] Levy, R., "Design Considerations for Lumped-Element Microwave Filters," *Microwave J.*, Vol. 31, February 1988, pp. 183–192.
- [12] Dayal, H., and Q. Le, "Printed Inductors on Alumina Substrates," *IEEE Microwave Magazine*, Vol. 2, June 2001, pp. 78–86.
- [13] Barinov, A. E., et al., "Superconducting Lumped-Element Filter with Spiral Inductors," *Microwave Opt. Lett.*, Vol. 29, April 2001, pp. 94–95.
- [14] Ong, C. K., et al., "High-Temperature Superconducting Bandpass Spiral Filters," *IEEE Microwave Guided Wave Lett.*, Vol. 9, October 1999, pp. 407–409.
- [15] Bhartia, P., and I. J. Bahl, *Millimeter Wave Engineering and Applications*, New York: John Wiley, 1984, Chap. 7.
- [16] Levy, R., *Directional Couplers in Advances in Microwaves*, Vol. 1, New York: Academic Press, 1966, pp. 184–191.
- [17] Davis, W. A., *Microwave Semiconductor Circuit Design*, New York: Van Nostrand Reinhold, 1983.
- [18] Malherbe, J. A. G., *Microwave Transmission Line Couplers*, Norwood, MA: Artech House, 1988.
- [19] Uysal, S., *Nonuniform Line Microstrip Directional Couplers and Filters*, Norwood, MA: Artech House, 1993.
- [20] Mongia, R., I. Bahl, and P. Bhartia, *RF and Microwave Coupled-Line Circuits*, Norwood, MA: Artech House, 1999.

-
- [21] Hirota, T., A. Minakawa, and M. Muraguchi, "Reduced-Size Branch-Line and Rat-Race Hybrids for Uniplanar MMICs," *IEEE Trans. Microwave Theory Tech.*, Vol. MTT-38, March 1990, pp. 270–275.
- [22] Coulton, M., et al., "Status of Lumped Elements in Microwave Integrated Circuit—Present and Future," *IEEE Trans. Microwave Theory Tech.*, Vol. MTT-19, July 1991, pp. 588–599.
- [23] Fusco, V. F., and S. B. D. O’Caireallain, "Lumped Element Hybrid Networks for GaAs MMICs," *Microwave Optical Tech. Lett.*, Vol. 2, January 1989, pp. 19–23.
- [24] Lu, L. H., et al., "Design and Implementation of Micromachined Lumped Quadrature (90°) Hybrids," *IEEE MTT-S Int. Microwave Symp. Dig.*, 2001, pp. 1285–1288.
- [25] Parisi, S. J., "A Lumped Element Rat Race Coupler," *Applied Microwave*, August/September 1989, pp. 84–93.
- [26] Hagerheiden, J., M. Ciminera, and G. Jue, "Improved Planar Spiral Transformer Theory Applied to a Miniature Lumped Element Quadrature Hybrid," *IEEE Trans. Microwave Theory Tech.*, Vol. 45, April 1997, pp. 543–545.
- [27] Shibata, K., "Microstrip Spiral Directional Coupler," *IEEE Trans. Microwave Theory Tech.*, Vol. MTT-29, July 1981, pp. 680–689.
- [28] McWhorter, M., "Broadband RF Transformer Directional Couplers," *RF Design*, July 1991, pp. 59–61.
- [29] Ellis, M. G., "RF Directional Couplers," *RF Design*, February 1997, pp. 30–43.
- [30] Directional Couplers, Brooklyn, NY: Mini-Circuits.
- [31] Wilkinson, E. J., "An N-Way Hybrid Power Divider," *IRE Trans. Microwave Theory Tech.*, Vol. MTT-8, January 1960, pp. 116–118.
- [32] Parad, L. I., and R. L. Moynihan, "Split-Tee Power Divider," *IEEE Trans. Microwave Theory Tech.*, Vol. MTT-13, January 1965, pp. 91–95.
- [33] Kopp, B., "Asymmetric Lumped Element Power Splitters," *IEEE MTT-S Int. Microwave Symp. Dig.*, 1989, pp. 333–336.
- [34] Staudinger, J., "Wide Bandwidth MMIC Power Dividers: Implementation and a Practical Design Technique," *Microwave J.*, Vol. 33, February 1990, pp. 73–90.
- [35] Chakmanlan, J. S., "Control VSWR Bandwidth in T-Section Networks," *Microwaves*, Vol. 20, July 1981, pp. 87–94.
- [36] Abrie, P. D., *Design of RF and Microwave Amplifiers and Oscillators*, Norwood, MA: Artech House, 1999, Chap. 7.
- [37] Davis, W. A., and K. K. Agarwal, *Radio Frequency Circuit Design*, New York: John Wiley, 2001.
- [38] White, J. F., *Microwave Semiconductor Engineering*, New York: Van Nostrand Reinhold, 1982.
- [39] Wolff, E. A., and R. Kaul, *Microwave Engineering and Systems Applications*, New York: John Wiley, 1988, Chap. 12.

- [40] Chang, K., (Ed), *Handbook of Microwave and Optical Components*, Vol. 2, New York: John Wiley, 1990, Chaps. 4 and 5.
- [41] Chang, K., *Microwave Solid-State Circuits and Applications*, New York: John Wiley, 1997.
- [42] Sharma, A. K., "Solid-State Control Devices: State of the Art," *Microwave J.*, September 1989, pp. 95–112.
- [43] Chang, K., I. Bahl, and V. Nair, *RF and Microwave Circuit and Component Design for Wireless Systems*, New York: John Wiley, 2002, Chap. 7.
- [44] Blackwell, D. A., D. E. Dawson, and D. C. Buck, "X-Band MMIC Switch with 70 dB Isolation and 0.5 dB Insertion Loss," *Microwave J.*, 1995, pp. 97–98.
- [45] Imai, N., A. Minakawa, and H. Ozaki, "Novel High-Isolation FET Switches," *IEEE Trans. Microwave Theory Tech.*, Vol. 44, May 1996, pp. 685–691.
- [46] Tokumitsu, T., I. Toyoda, and M. Aikawa, "A Low-Voltage, High-Power T/R Switch MMIC Using LC Resonators," *IEEE Trans. Microwave Theory Tech.*, Vol. 43, May 1995, pp. 997–1003.
- [47] Ayasli, Y., et al., "Wide-Band Monolithic Phase Shifter," *IEEE Trans. Microwave Theory Tech.*, Vol. 32, December 1984, pp. 1710–1714.
- [48] Moye, C., G. Sakamoto, and M. Brand, "A Compact Broadband, Six-Bit MMIC Phasor with Integrated Digital Drivers," *IEEE Microwave and Millimeter-Wave Monolithic Circuits Symp. Dig.*, 1990, pp. 123–126.
- [49] Krafcsik, D. M., et al., "A Low-Loss X-Band 6-Bit MMIC Phase Shifter Using MESFET Switches," *GOMAC Dig.*, 1991, pp. 355–358.
- [50] Wallace, J., H. Redd, and R. Furlow, "Low Cost MMIC DBS Chip Sets for Phased Array Applications," *IEEE MTT-S Int. Microwave Symp. Dig.*, 1999, pp. 677–680.
- [51] Campbell, C. F., and S. A. Brown, "A Compact 5-Bit Phase Shifter MMIC for K-Band Satellite Communication Systems," *IEEE Trans. Microwave Theory Tech.*, Vol. 48, December 2000, pp. 2652–2656.